

# Investigation of Ca Insertion into $\alpha$ -MoO<sub>3</sub> Nanoparticles for High Capacity Ca-Ion Cathodes

Sanghyeon Kim, Liang Yin, Seong-Min Bak, Timothy T. Fister, Haesun Park, Prakash Parajuli, Jihyeon Gim, Zhenzhen Yang, Robert F. Klie, Peter Zapol, Yonghua Du, Saul H. Lapidus, and John T. Vaughey\*

Cite This: *Nano Lett.* 2022, 22, 2228–2235

Read Online

ACCESS |

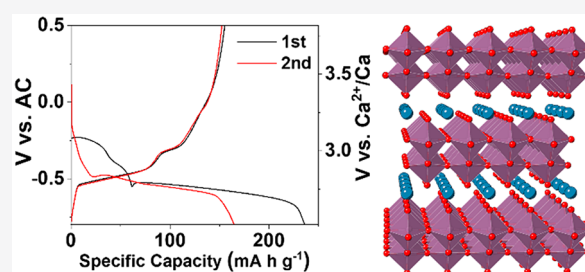
Metrics & More

Article Recommendations

Supporting Information

**ABSTRACT:** Calcium-ion batteries (CIBs) are a promising alternative to lithium-ion batteries (LIBs) due to the low redox potential of calcium metal and high abundance of calcium compounds. Due to its layered structure,  $\alpha$ -MoO<sub>3</sub> is regarded as a promising cathode host lattice. While studies have reported that  $\alpha$ -MoO<sub>3</sub> can reversibly intercalate Ca ions, limited electrochemical activity has been noted, and its reaction mechanism remains unclear. Here, we re-examine Ca insertion into  $\alpha$ -MoO<sub>3</sub> nanoparticles with a goal to improve reaction kinetics and clarify the storage mechanism. The  $\alpha$ -MoO<sub>3</sub> electrodes demonstrated a specific capacity of 165 mA h g<sup>-1</sup> centered near 2.7 V vs Ca<sup>2+</sup>/Ca, stable long-term cycling, and good rate performance at room temperature. This work demonstrates that, under the correct conditions, layered oxides can be a promising host material for CIBs and renews prospects for CIBs.

**KEYWORDS:** multivalent batteries, calcium-ion batteries, layered structure, oxides, cathode materials, nanomaterials



Lithium-ion batteries (LIBs) have been the dominant energy storage system for portable electronics, consumer goods, and electric vehicles for nearly 30 years.<sup>1,2</sup> However, concerns regarding the costs of isolating the needed lithium sources, safety issues, and new portable power applications have led to an active search for beyond lithium-ion technologies.<sup>3,4</sup> Among these chemistries, energy storage systems based on multivalent charge carriers have received considerable attention as they have higher theoretical energy densities than LIBs when used in conjunction with metal anodes.<sup>3–5</sup> Among the many multivalent battery systems (such as Al<sup>3+</sup>, Ca<sup>2+</sup>, Mg<sup>2+</sup>, Zn<sup>2+</sup>), calcium-ion batteries (CIBs) are one of the most promising candidates due to the low reduction potential of calcium (–2.87 V vs standard hydrogen electrode), safety (no dendrite formation), and the high elemental abundance of calcium.<sup>6,7</sup> However, to date, a CIB cathode with high energy density and Coulombic efficiency has not been demonstrated. While a full cell CIB requires a working Ca metal anode, that advance was only recently demonstrated,<sup>8–12</sup> and the discovery of stable and high energy density calcium ion cathodes is still required to achieve practical energy density values for CIBs.

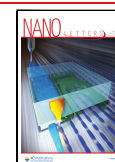
Orthorhombic  $\alpha$ -MoO<sub>3</sub> is a compelling cathode candidate, as it is a well-known intercalation host for monovalent and multivalent cations and has a stable layered structure known to intercalate a variety of guest ions.<sup>13–25</sup> Additionally, highly ionic oxide frameworks typically enable higher cell voltages compared to those built using soft anions (i.e., S, Se)<sup>26</sup> while

providing good structural stability during cycling. Ca-ion intercalation into  $\alpha$ -MoO<sub>3</sub> was first reported in 2018<sup>24,25</sup> using micrometer-scale bulk and ball-milled particles. Although the delivered capacities were attributed to Ca intercalation, some major issues remain unsolved. They showed featureless discharge curves with no clear reaction voltage plateaus while exhibiting large voltage hysteresis with specific capacities not in line with the predicted theoretical capacity (186 mA h g<sup>-1</sup> assuming one electron reaction; Ca<sub>0.5</sub>MoO<sub>3</sub>) at a reasonable current density. This may be related to sluggish Ca<sup>2+</sup> diffusion within the lattice since the divalent charge of the Ca<sup>2+</sup> ion has a strong Coulombic interaction with other ions in the framework, leading to high activation energy barrier. This reaction kinetic issue can be addressed by reducing the particle size of the cathode material to the nanoscale to provide shorter Ca<sup>2+</sup> diffusion pathways and increase the amount of the electrode surface exposed to the electrolyte.<sup>27,28</sup> Previous studies suggest that ball milling may not be an ideal method to reduce the particle size of bulk material because it can damage the structure of the material and affect its electrochemical

**Received:** October 27, 2021

**Revised:** February 2, 2022

**Published:** March 2, 2022



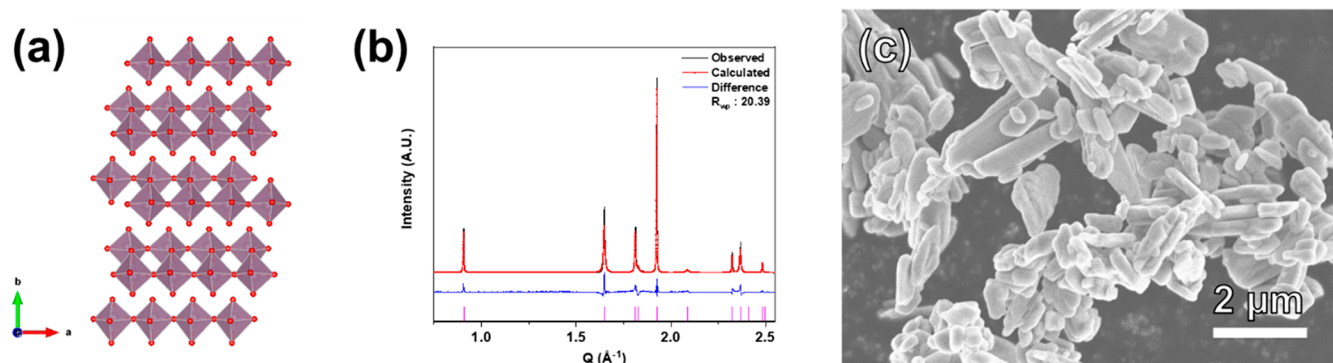


**Figure 1.** (a) Crystal structure, (b) synchrotron XRD patterns and Rietveld refinement, and (c) SEM image of  $\alpha$ -MoO<sub>3</sub> nanoparticles.

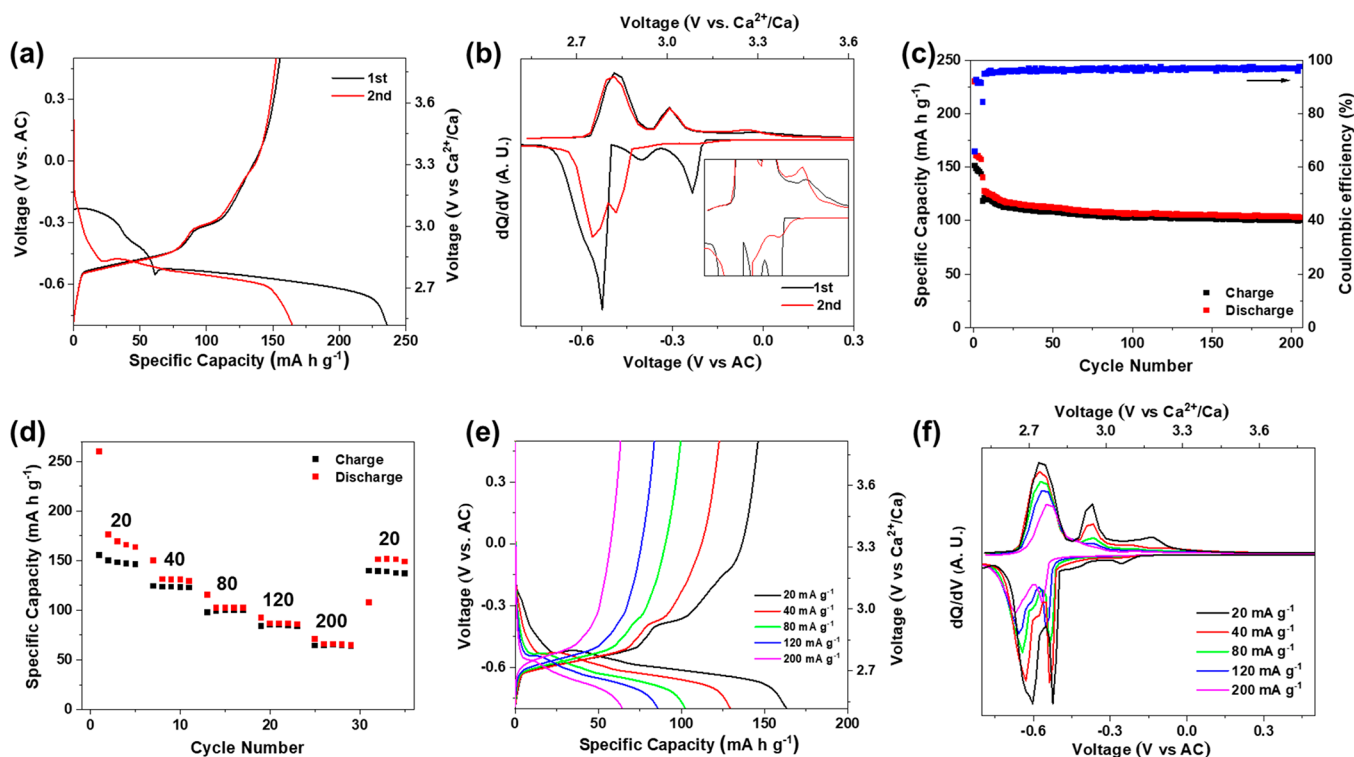


**Figure 2.** (a) 1st and 2nd cycle galvanostatic discharge–charge curves of  $\alpha$ -MoO<sub>3</sub> nanoparticles at 20 mA h<sup>−1</sup> at room temperature. (b) Corresponding differential capacity plot for Figure 2a. The inset shows a magnified view. (c) Cycling performance of  $\alpha$ -MoO<sub>3</sub> nanoparticles at 40 mA g<sup>−1</sup> after 5 cycles at 20 mA h<sup>−1</sup> at room temperature. (d) Rate performance of  $\alpha$ -MoO<sub>3</sub> nanoparticles at different *c*-rates ranging from 20 mA g<sup>−1</sup> to 200 mA g<sup>−1</sup> at room temperature. (e) Galvanostatic discharge–charge curves of  $\alpha$ -MoO<sub>3</sub> nanoparticles at different *c*-rates. (f) Corresponding differential capacity plot for part (e).

performance negatively. Thus, better performance is expected when materials are synthesized directly. Also, as  $\alpha$ -MoO<sub>3</sub> is a relatively cation agnostic host material, a more detailed characterization suite needs to be done to confirm Ca<sup>2+</sup> insertion. This is important to the beyond Li-ion field as cointercalation of other ions or side reactions can occur that contributes to the observed reversible electrochemical reactions. Thus, it is significant to observe the necessary changes rather than claiming Ca intercalation based purely on electrochemical data. There has been only one report of using hydrated MoO<sub>3</sub> for the Ca cathode.<sup>29</sup> Although it showed a high specific capacity at room temperature, lattice water in the host structure lowers volumetric energy density and could exchange with the electrolyte solvent, leading to side reactions, anode passivation, and salt degradation. Since the ability of a dehydrated  $\alpha$ -MoO<sub>3</sub> to accommodate Ca<sup>2+</sup> is still not fully

understood, further mechanistic studies are required to understand the storage pathways and charge compensation mechanisms.

Here, we evaluated  $\alpha$ -MoO<sub>3</sub> nanoparticles as CIB cathodes in order to address the issues associated with the extent of intercalation and the mechanism of insertion. In this study, it was found that a nanoscaled  $\alpha$ -MoO<sub>3</sub> reversibly cycles Ca ions in nonaqueous electrolyte at room temperature. The mechanism of electrochemical Ca insertion into  $\alpha$ -MoO<sub>3</sub> nanoparticles was investigated using multimodal X-ray synchrotron techniques including high resolution X-ray diffraction (XRD), X-ray absorption spectroscopy (XAS), and X-ray fluorescence (XRF) imaging and density functional theory (DFT) calculations.

Figure 1a shows the orthorhombic layered structure of  $\alpha$ -MoO<sub>3</sub> consisting of two octahedral [MoO<sub>6</sub>] layers joined by

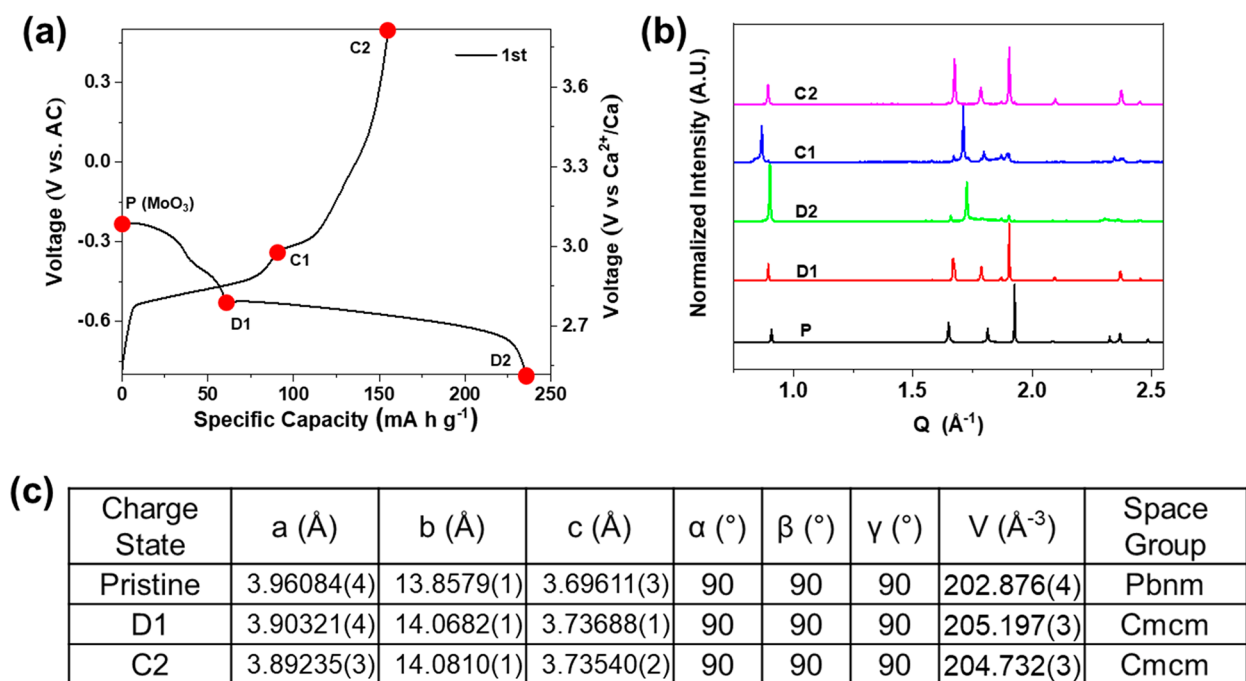


**Figure 3.** (a) Indication of various stages during the first cycle where the ex situ sample was prepared. (b) Ex situ synchrotron XRD patterns of  $\alpha$ -MoO<sub>3</sub> nanoparticles at four states of charge. (c) Cell parameters from Rietveld refinement and Pawley fitting results for  $\alpha$ -MoO<sub>3</sub> nanoparticles at pristine, D1, and C2 states.

an edge (along the [100] direction) and corner (along the [001] direction). These planes are alternately stacked and separated by weak van der Waals attraction forces along the [010] direction where guest ions can be easily accommodated between the layers. The framework Mo<sup>6+</sup> cations are reduced to balance the charges. Rietveld refinements of synchrotron diffraction data of the  $\alpha$ -MoO<sub>3</sub> nanoparticles confirmed the space group of orthorhombic *Pbnm* (Figure 1b). The scanning electron microscope (SEM) image of  $\alpha$ -MoO<sub>3</sub> nanoparticles (Figure 1c) shows irregular nanorod morphology with a width of 150–200 nm.

The  $\alpha$ -MoO<sub>3</sub> nanoparticle electrodes were examined as Ca-ion electrodes using galvanostatic discharge/charge tests. The capacitive AC electrode was used and functions as a quasi-reference electrode in that the potential of an AC electrode is stable.<sup>30</sup> The electrodes were not discharged below 2.5 V vs Ca<sup>2+</sup>/Ca to avoid possible conversion reactions or side reactions in the low voltage region. The thermodynamic potential of the conversion reaction was calculated to be 2.58 V vs Ca<sup>2+</sup>/Ca based on the formation energies. Figure 2a shows the  $\alpha$ -MoO<sub>3</sub> electrode delivered 236 and 165 mA h g<sup>-1</sup> at a current density of 20 mA g<sup>-1</sup> for the first discharge and charge capacity, respectively, with 83 mA h g<sup>-1</sup> irreversible capacity in the first cycle, which will be discussed later. This irreversible capacity is no longer observed after the first cycle.<sup>31</sup> The  $\alpha$ -MoO<sub>3</sub> electrode reversibly delivered a specific capacity of 165 mA h g<sup>-1</sup> (discharge capacity basis), corresponding to 0.44 mol of Ca<sup>2+</sup>/MoO<sub>3</sub>. The discharge–charge curves of the  $\alpha$ -MoO<sub>3</sub> electrode show multiple plateaus suggesting the stepwise reactions, similar to previously observed behavior of  $\alpha$ -MoO<sub>3</sub> in Li and Ca intercalation cases.<sup>17,18,24,25</sup> The specific capacity was centered around a 2.7 V vs the Ca<sup>2+</sup>/Ca plateau. Some potential jump phenomena were observed in the first and second discharge curves, as previously seen in Zn intercalation into  $\alpha$ -MoO<sub>3</sub>,<sup>22</sup> and they have been attributed

to electrode phase transitions based on lattice layer shifts and/or cation reordering, which takes some time to reach equilibrium. The multiple phase reactions are clearly seen in the dQ/dV curve with several cathodic and anodic peaks (Figure 2b). After the first cycle, the reduction peaks at 2.7, 2.8, and 3.1 V vs Ca<sup>2+</sup>/Ca and oxidation peaks at 2.8, 3, and 3.3 V vs Ca<sup>2+</sup>/Ca were shown, respectively, suggesting three redox peak pairs. The differences between each redox peak are 0.08, 0.18, and 0.18 V, indicating small voltage hysteresis. These values are significantly smaller when compared to the previously reported MoO<sub>3</sub> studies for CIB (Table S1). We suspect concentration polarization originating from limitations in diffusion was improved in moving to smaller particle sizes which leads to smaller voltage hysteresis. The  $\alpha$ -MoO<sub>3</sub> electrode showed stable capacity retention and delivered a discharge capacity of 103 mA h g<sup>-1</sup> after 200 cycles at 40 mA g<sup>-1</sup> (Figure 2c). Furthermore, the Coulombic efficiency of the electrode stabilizes around 97.5% through 200 cycles. The discharge–charge curves of the  $\alpha$ -MoO<sub>3</sub> electrode for subsequent cycles during long-term cycling are presented in Figure S1. Based on the charge–discharge curves and data analysis, the reaction mechanism appears to remain consistent after first cycle once the *t* overpotential increase in the initial cycles is taken into account. Specific capacities of 163, 129, 102, 86, and 64 mA h g<sup>-1</sup> (fifth discharge capacity at each current density) were achieved at 20, 40, 80, 120, and 200 mA g<sup>-1</sup>, respectively (Figure 2d). When the rate returns to 200 mA g<sup>-1</sup> from 20 mA g<sup>-1</sup>, the discharge capacity recovered to 151 mA h g<sup>-1</sup> (93% retention). The discharge–charge curves and the dQ/dV curves (Figure 2e,f) at high current densities still showed clear electrochemical reactions, and the voltage hysteresis did not increase significantly, indicating good reaction kinetics. The improved reaction kinetics can be attributed to small diffusion distances seen in the  $\alpha$ -MoO<sub>3</sub> nanoparticles.<sup>27,28</sup> The results presented here are useful to

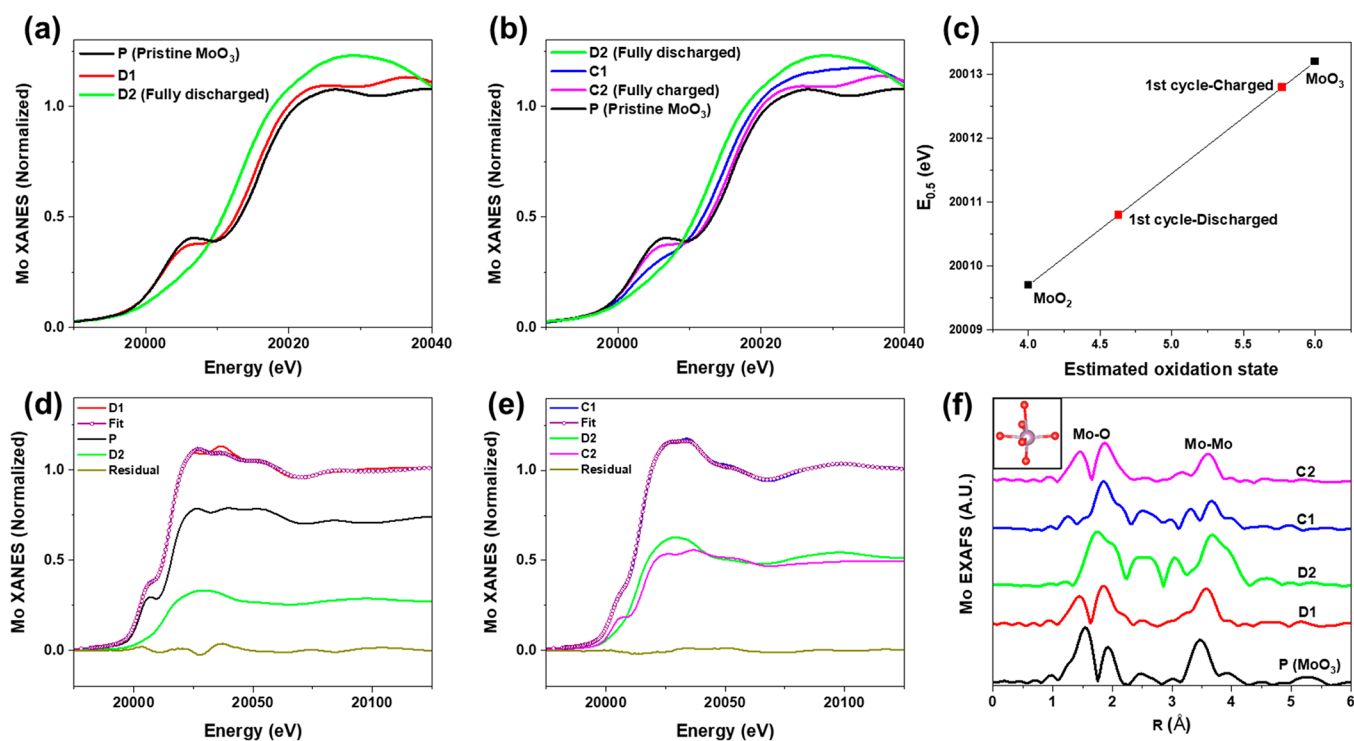


**Figure 4.** Ex situ Mo K-edge XANES spectra of  $\alpha$ -MoO<sub>3</sub> nanoparticles at different states of charge during (a) discharge and (b) charge. (c) Estimation of the oxidation state of Mo in  $\alpha$ -MoO<sub>3</sub> nanoparticles before cycling and after discharge and charge using the Mo K-edge energy (at half height of normalized XANES spectra) shift. Linear combination fit for (d) D1 and (e) C1. Ex situ (f) Mo K-edge EXAFS spectra of  $\alpha$ -MoO<sub>3</sub> at different states of charge (phase is not corrected). The inset shows a distorted MoO<sub>6</sub> octahedron of pristine of  $\alpha$ -MoO<sub>3</sub>.

consider molybdenum oxide host lattices as a possible CIB cathode system. The voltage difference (overpotential) between the charge/discharge potential and the quasi-equilibrium potential in the galvanostatic intermittent titration technique (GITT) is plotted in Figure S2c. It shows that the region where the potential jump phenomena appeared exhibited a larger polarization than the redox reaction of the main voltage plateau, suggesting that the energy barrier of redox reaction at higher voltage is higher than that of the redox reaction at lower voltage. Even though direct comparison may not be suitable due to different particle sizes and different electrolytes, the overpotential was compared with that of  $\alpha$ -MoO<sub>3</sub> in LIB,<sup>31</sup> and the  $\alpha$ -MoO<sub>3</sub> nanoparticles in a Ca cell showed a comparable or even smaller polarization, indicating the enhanced reaction kinetics.

Ex situ XRD was performed with the electrodes discharged to D1 and D2 and charged back to C1 and C2 during the first cycle as marked on the charge–discharge curve (boundaries were made based on the respective redox reaction/plateau). These ex situ samples were further used for other characterization studies after it was noted that  $\alpha$ -MoO<sub>3</sub> showed a distinct phase transition during cycling (Figure 3b). Due to the difficulty in identifying the phase of the D2 and C1 samples, Pawley fitting was only applicable for D1 and C2 samples. The pristine sample is a typical orthorhombic  $\alpha$ -MoO<sub>3</sub> with a space group of *Pbnm* (No. 62). Upon discharge, the symmetry of the orthorhombic lattice changes (Figure 3b) and the discharged D1 phase can be indexed with space group *Cmcm* (No. 63). On further discharging, the formation of new phases can be seen in the high-resolution XRD of sample D2. The identification of new phases is challenging due to the complexity of the reflections. However, a strong and sharp

reflection is observed around 0.9 Å<sup>-1</sup>, which is similar to the (020) reflection in the XRD of pristine and D1 samples. Since the (020) peaks correspond to the layering reflection in the stacking direction of the MoO<sub>6</sub> layers, this new structure may result from the gliding of MoO<sub>6</sub> layers, which reduces the extent of ordering in the *a/b* direction. The phase transition from the *Cmcm* phase to new structures is reversible. A trace amount of the *Cmcm* phase can be observed in the charged sample C1. After further charging, the *Cmcm* phase is fully recovered as seen in the XRD data of sample C2. However, even charged up to 3.8 V vs Ca<sup>2+</sup>/Ca, the cathode is still not fully recovered to the pristine state. This is perhaps due to trapped inserted Ca<sup>2+</sup> in the MoO<sub>3</sub> or the electrode undergoing irreversible structural changes such as defect generation (anion loss) or layer rearrangement, accounting for irreversible capacity during the first cycle.<sup>24</sup> The unit cell parameters and volumes of P (pristine), D1, and C2 samples extracted from Rietveld refinements or Pawley fitting are summarized in Figure 3c.  $\alpha$ -MoO<sub>3</sub> electrodes showed an irreversible structural change that does not seem to be related to a conversion reaction as any phase expected to be a product of the conversion reaction (Mo, MoO<sub>2</sub>, CaO) was not identified while the high level of crystallinity of the host materials was maintained during the charge and discharge. Reaction mechanisms that are associated with a conversion reaction are typically accompanied by a loss in crystallinity. No significant volume expansion or morphology changes were observed during cycling, indicating intercalation is the predominant reaction mechanism rather than a conversion reaction (Figure S4). The structure evolution after the first cycle was examined by ex situ XRD with twice cycled electrodes (Figure S5). It was confirmed that the first cycle

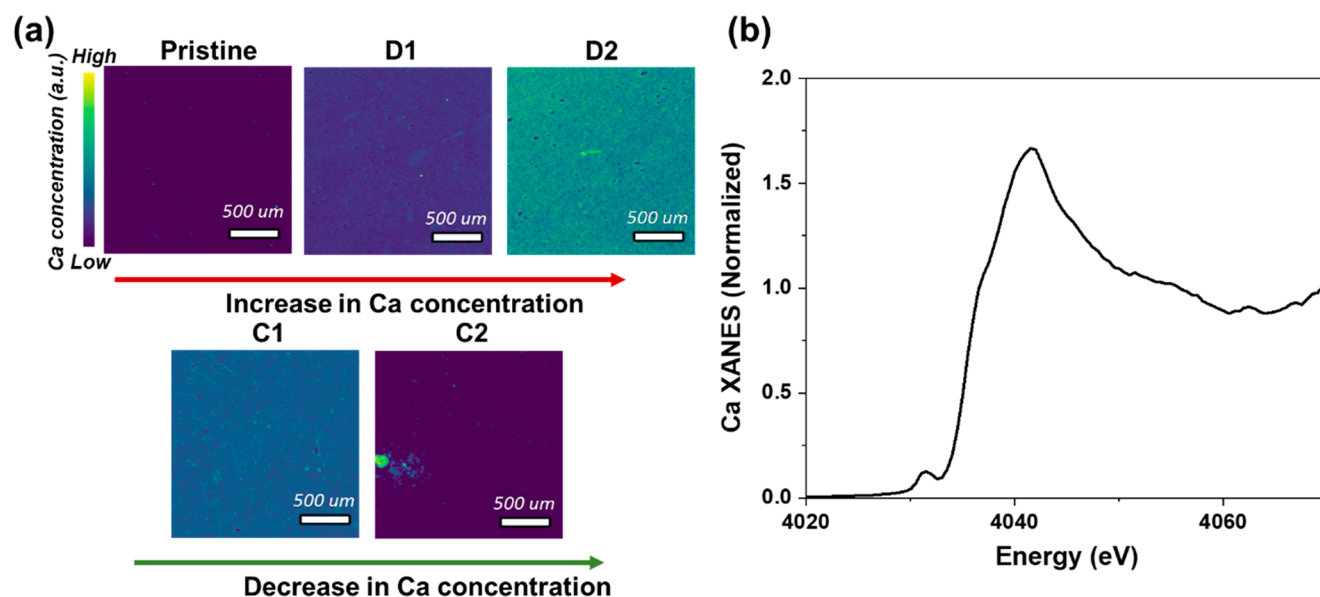


**Figure 5.** (a) XRF mapping of Ca in electrodes at different states of charge with an incident beam energy of 4.3 keV. (b) Normalized Ca K-edge XANES spectrum measured from D2 (fully discharged).

irreversible structural change only occurred in the first cycle and that the phase transition after the first cycle seems to have remained the same for the subsequent cycles, which is in good agreement with discharge–charge curves of the following cycles (Figure S1).

One thing to note is that the (020) peak shifted toward higher  $q$  from D1 to D2 during discharge and shifted back toward lower  $q$  from D2 to C1 during charge. This change in  $d$ -spacing of the interlayer decreases with Ca insertion and increases with Ca deinsertion in the lower voltage plateau, which is contrary to the typical intercalation behavior of other layered electrodes where a measurable expansion of the interlayer spacing was observed. However, this crystallographic behavior has previously been reported for  $\alpha$ - $\text{MoO}_3$  in the low voltage region for Li intercalation cases,  $\text{Li}_x[\text{MoO}_3]$ , and appears to be associated with its complex intercalation mechanism.<sup>15,32</sup>

Figure S6b shows DFT-calculated structures of  $\text{Ca}_1\text{Mo}_{36}\text{O}_{108}$  ( $\text{Ca}_{0.03}\text{MoO}_3$ ) with a single Ca ion occupying various possible Ca sites and their formation energies. The  $\text{Ca}_1\text{Mo}_{36}\text{O}_{108}$  composition was chosen for balancing the representation of the dilute Ca concentration and affordable simulation cell size. The formation energies for Ca intercalation into three symmetrically distinctive sites in  $\alpha$ - $\text{MoO}_3$  are negative, and the values are nearly constant over these Ca intercalation sites. Either the Ca ion occupies the channel within the  $[\text{MoO}_6]$  octahedra layer in one of the sites (intralayer position) or Ca resides between  $\text{MoO}_6$  layers in the other two sites (interlayer position). For the interlayer positions, Ca sites are distinguished by different Ca–O coordination environments. As demonstrated by DFT calculation, the formation energies for Ca occupying inter- and intralayer positions are almost the same, which indicates that Ca can occupy both inter- and intralayer positions. Notably, Ca intercalation into the intralayer position can complicate the stacking order between Mo–O octahedra layers or affect the linkage of Mo–O octahedra layers.<sup>15</sup> In this case,  $d$ -spacing in the interlayer can decrease with Ca intercalation,

which happened from D1 to D2 during discharge and vice versa during charge.

Figure 4a,b shows the Mo K-edge X-ray absorption near edge structure (XANES) spectra of  $\alpha$ - $\text{MoO}_3$  at different charge states during cycling. A pre-edge peak is observed in pristine  $\alpha$ - $\text{MoO}_3$ , which is due to the transition from the 1s to the 4d orbital.<sup>33</sup> The octahedral oxygen coordination is greatly distorted in  $\alpha$ - $\text{MoO}_3$  because the  $\text{MoO}_6$  octahedron consists of four shorter Mo–O bonds and two much longer Mo–O bonds (the inset in Figure 4f). This induces the Mo  $s$ – $d$  excitation, resulting in a pre-edge peak in the Mo K-edge spectra. However, the intensity of the pre-edge peak decreases on discharge and disappears when the electrode is discharged to the D2 state. This suggests that the Mo–O coordination environment is less distorted in Ca discharged  $\alpha$ - $\text{MoO}_3$ . The pre-edge peak reappeared during the charging process. The position of the main edge corresponding to a 1s  $\rightarrow$  5p transition is sensitive to the Mo oxidation state. The Mo K-edge shifted toward lower energies gradually due to the reduction of  $\text{Mo}^{6+}$  as the  $\alpha$ - $\text{MoO}_3$  electrode is discharged. After charging, the Mo K-edge shifted back to higher energies, and the edge closely returns to the original position of  $\alpha$ - $\text{MoO}_3$ , indicating the reversible reduction and oxidation of Mo. The oxidation state of Mo in the D2 and C2 states was estimated assuming the linear correlation between the edge energy and average oxidation state (Figure 4c).<sup>34,35</sup> The energy at half the height of normalized XANES spectra, which corresponds to continuum state transitions above the pre-edge orbital, was used to define the edge position. Based on this shift (Figure 4c) and the position of  $\text{Mo}^{4+}$  and  $\text{Mo}^{6+}$  standards, the Mo oxidation states in the D2 and C2 states were determined to be roughly 4.6+ and 5.8+, respectively, indicating the electrochemical redox reaction contributes to the reversible capacity of  $\alpha$ - $\text{MoO}_3$  mostly. A linear combination fit of XANES spectra of intermediate states during discharge and charge. The spectra of the D1 and C1 can be regarded as a linear combination of the end phases (discharged and charged states). The XANES spectra of D1

and C1 were fitted by using a linear combination of P/D2 and D2/C2, respectively (Figure 4d,e). According to the linear combination fit, D1 is composed of 73% of P and 27% of D2 and C1 is composed of 51% of D2 and 49% of C2, which is generally consistent with state of charges of D1 and C1 calculated based on electrochemical charge/discharge profiles. In the Fourier transformed extended X-ray absorption fine structure (EXAFS) (Figure 4f), the peaks below 2 Å (phase is not corrected) can be assigned to Mo–O bonds, and the peaks from 3 to 4 Å can be assigned to Mo–Mo interactions. The Mo–O peaks gradually merge during discharge. The amplitude increase for  $\alpha$ -MoO<sub>3</sub> suggests that first neighboring oxygen atoms are rearranged and the noncentrosymmetric nature of the Mo–O environment is mitigated upon discharge, which is consistent with the disappearance of a pre-edge peak in XANES. In the D2 state, a new coordination shell just above 2 Å (2.5 Å phase-shifted) appears in the second and third shells. This could be due to scattering paths from calcium sites or a rearrangement of Mo upon deep Ca intercalation to a local coordination approaching a lower oxidation state of the Mo cations. The formation of shorter Mo–Mo interactions was previously reported for the case of Li intercalation into  $\alpha$ -MoO<sub>3</sub>.<sup>36</sup> After charging, the EXAFS spectrum of C2 was recovered and found to closely match the pristine (uncycled) sample, indicating good local structure reversibility.

Figure 5a shows Ca-ion concentration increases during discharge and decreases during charge as expected. The electrodes show a uniform Ca-ion distribution, indicating Ca-ion insertion and deinsertion occur homogeneously at the electrode level with the nanoparticle-based electrodes used for this study. The Ca K-edge XANES spectrum of D2 (fully discharged), which is highly sensitive to the local environment, is shown in Figure 5b.<sup>37</sup> The direct comparison between chemically calcinated Ca<sub>0.5</sub>MoO<sub>3</sub> and electrochemically prepared electrodes would be the most ideal, but unfortunately, it was not possible as we were unable to synthesize or acquire chemically calcinated samples. Instead, the XANES spectrum of D2 was compared with electrolyte precipitate. A sample for electrolyte precipitate was prepared by dipping the electrode into the electrolyte and drying it (Figure S7). The spectrum from the electrode was different from that from electrolyte precipitate (i.e., Ca(TFSI)<sub>2</sub>), where Ca exists on the surface. Also, a pre-edge peak was observed due to the transition from the 1s to 3d orbital, which occurs when Ca is not in a centrosymmetric environment. This is opposite to the absence of the pre-edge peak in the Ca K-edge XANES spectrum of CaO,<sup>38</sup> suggesting it is not a conversion reaction. The atomic ratio of Ca/Mo based on the energy-dispersive X-ray spectroscopy (EDS) quantification results and calculated from the discharge and charge capacity of the EDS samples is shown in Table S2. It showed a similar tendency to the electrochemical capacity; however, much less Ca was detected from the fully charged samples, suggesting the irreversible capacity in the first cycle may not fully consist of Ca intercalation and may contain other contributions from side reactions, notably electrolyte decomposition. Based on the X-ray photoelectron spectroscopy (XPS) data (Figure S9), it was confirmed that a cathode electrolyte interphase layer was formed and that it mainly contained C–C, C–O (organic species from solvent), and Ca–O species. The data is consistent with the TFSI<sup>−</sup> salt itself being stable, as estimated from the S 2p peak, which is consistent with XRF data. We suspect that this electrolyte decomposition and formation of

the electrolyte interphase during discharge may contribute to relatively low Coulombic efficiency.

In conclusion,  $\alpha$ -MoO<sub>3</sub> as a practical Ca electrode material was re-examined using nanoparticles. The  $\alpha$ -MoO<sub>3</sub> nanoparticles were found to reversibly cycle Ca ions, while the electrode showed good long-term cyclability, good rate performance, and small hysteresis at high current density. The improved electrochemical performance of  $\alpha$ -MoO<sub>3</sub> versus previously reported studies may be attributable to the enhanced reaction kinetics accessed by going to a nanoscale particle as it reduces the electron and ion diffusion lengths. While we have yet to do the experiments, we suspect the specific capacity of  $\alpha$ -MoO<sub>3</sub> can be further increased by preparing smaller nanoparticles with fewer defects, which may also tell us if a size-dependent Ca storage mechanism in Mo-based oxides exists. This study suggests that resolving the rate limiting issues is an important step for the future design of multivalent batteries and investigating new electrode materials. The consistent changes in structure, electronic environment, and chemical composition were observed during cycling, indicating Ca can reversibly be inserted into and deinserted from  $\alpha$ -MoO<sub>3</sub>. The main reaction mechanism appears to be an intercalation reaction that is initiated with an irreversible structural change in the first cycle. We believe this result shows a significant advance compared to previously reported oxide-based materials for CIBs and satisfies a significant milestone in the search for practical Ca batteries.

## ■ ASSOCIATED CONTENT

### Supporting Information

The Supporting Information is available free of charge at <https://pubs.acs.org/doi/10.1021/acs.nanolett.1c04157>.

Galvanostatic discharge–charge curves of subsequent cycles, GITT curves, Pawley fitting of ex situ  $\alpha$ -MoO<sub>3</sub> electrodes, ex situ SEM images of  $\alpha$ -MoO<sub>3</sub> nanoparticles, ex situ synchrotron XRD patterns of 2nd cycled samples, various possible Ca sites predicted by DFT calculations, XRF mapping of Ca in a control sample and the corresponding normalized Ca K-edge XANES spectrum, differential capacity plots for delithiation of LiFePO<sub>4</sub> in different types of cells, XPS analysis for  $\alpha$ -MoO<sub>3</sub> electrodes, voltage hysteresis comparison among previously reported MoO<sub>3</sub>-based Ca cathodes and those of the present work, and ex situ EDS results for  $\alpha$ -MoO<sub>3</sub> electrodes (PDF)

## ■ AUTHOR INFORMATION

### Corresponding Author

John T. Vaughey – Chemical Sciences and Engineering Division, Argonne National Laboratory, Lemont, Illinois 60439, United States; Joint Center for Energy Storage Research, Argonne National Laboratory, Lemont, Illinois 60439, United States; [orcid.org/0000-0002-2556-6129](https://orcid.org/0000-0002-2556-6129); Email: [vaughey@anl.gov](mailto:vaughey@anl.gov)

### Authors

Sanghyeon Kim – Chemical Sciences and Engineering Division, Argonne National Laboratory, Lemont, Illinois 60439, United States; Joint Center for Energy Storage Research, Argonne National Laboratory, Lemont, Illinois 60439, United States; [orcid.org/0000-0003-2789-449X](https://orcid.org/0000-0003-2789-449X)

Liang Yin – Joint Center for Energy Storage Research and X-ray Science Division, Advanced Photon Source, Argonne National Laboratory, Lemont, Illinois 60439, United States; [orcid.org/0000-0001-5396-782X](https://orcid.org/0000-0001-5396-782X)

Seong-Min Bak – National Synchrotron Light Source II, Brookhaven National Laboratory, Upton, New York 11973, United States; [orcid.org/0000-0002-1626-5949](https://orcid.org/0000-0002-1626-5949)

Timothy T. Fister – Chemical Sciences and Engineering Division, Argonne National Laboratory, Lemont, Illinois 60439, United States; Joint Center for Energy Storage Research, Argonne National Laboratory, Lemont, Illinois 60439, United States; [orcid.org/0000-0001-6537-6170](https://orcid.org/0000-0001-6537-6170)

Haesun Park – Joint Center for Energy Storage Research and Materials Science Division, Argonne National Laboratory, Lemont, Illinois 60439, United States; School of Integrative Engineering, Chung-Ang University, Seoul 06974, Republic of Korea

Prakash Parajuli – Joint Center for Energy Storage Research, Argonne National Laboratory, Lemont, Illinois 60439, United States; Department of Physics, University of Illinois at Chicago, Chicago, Illinois 60607, United States; [orcid.org/0000-0001-6732-2010](https://orcid.org/0000-0001-6732-2010)

Jihyeon Gim – Chemical Sciences and Engineering Division, Argonne National Laboratory, Lemont, Illinois 60439, United States

Zhenzhen Yang – Chemical Sciences and Engineering Division, Argonne National Laboratory, Lemont, Illinois 60439, United States; Joint Center for Energy Storage Research, Argonne National Laboratory, Lemont, Illinois 60439, United States

Robert F. Klie – Joint Center for Energy Storage Research, Argonne National Laboratory, Lemont, Illinois 60439, United States; Department of Physics, University of Illinois at Chicago, Chicago, Illinois 60607, United States; [orcid.org/0000-0003-4773-6667](https://orcid.org/0000-0003-4773-6667)

Peter Zapol – Joint Center for Energy Storage Research and Materials Science Division, Argonne National Laboratory, Lemont, Illinois 60439, United States; [orcid.org/0000-0003-0570-9169](https://orcid.org/0000-0003-0570-9169)

Yonghua Du – National Synchrotron Light Source II, Brookhaven National Laboratory, Upton, New York 11973, United States

Saul H. Lapidus – Joint Center for Energy Storage Research and X-ray Science Division, Advanced Photon Source, Argonne National Laboratory, Lemont, Illinois 60439, United States; [orcid.org/0000-0002-7486-4325](https://orcid.org/0000-0002-7486-4325)

Complete contact information is available at:  
<https://pubs.acs.org/10.1021/acs.nanolett.1c04157>

## Notes

The authors declare no competing financial interest.

## ACKNOWLEDGMENTS

This work was supported by the Joint Center for Energy Storage Research, an Energy Innovation Hub funded by the U.S. Department of Energy, Office of Science, Basic Energy Sciences. This research used resources of the Advanced Photon Source, a U.S. Department of Energy (DOE) Office of Science User Facility operated for the DOE Office of Science by Argonne National Laboratory under Contract No. DE-AC02-06CH11357. This work is conducted at Argonne National Laboratory supported by the U.S. Department of Energy under

Contract DE-A02-06CH11357. Use of the Center for Nanoscale Materials, an Office of Science user facility, was supported by the U.S. Department of Energy, Office of Science, Office of Basic Energy Sciences, under Contract No. DE-AC02-06CH11357. The XAS research used beamline 8-BM (TES) of the National Synchrotron Light Source II, a U.S. Department of Energy (DOE) Office of Science User Facility, operated for the DOE Office of Science by Brookhaven National Laboratory under Contract No. DE-SC0012704.

## REFERENCES

- (1) Etacheri, V.; Marom, R.; Elazari, R.; Salitra, G.; Aurbach, D. Challenges in the development of advanced Li-ion batteries: a review. *Energy Environ. Sci.* **2011**, *4*, 3243–3262.
- (2) Blomgren, G. E. The Development and Future of Lithium Ion Batteries. *J. Electrochem. Soc.* **2017**, *164*, A5019–A5025.
- (3) Ponrouch, A.; Bitenc, J.; Dominko, R.; Lindahl, N.; Johansson, P.; Palacin, M. R. Multivalent rechargeable batteries. *Energy Storage Mater.* **2019**, *20*, 253–262.
- (4) Canepa, P.; Sai Gautam, G.; Hannah, D. C.; Malik, R.; Liu, M.; Gallagher, K. G.; Persson, K. A.; Ceder, G. Odyssey of Multivalent Cathode Materials: Open Questions and Future Challenges. *Chem. Rev.* **2017**, *117*, 4287–4341.
- (5) Liu, M.; Rong, Z.; Malik, R.; Canepa, P.; Jain, A.; Ceder, G.; Persson, K. A. Spinel compounds as multivalent battery cathodes: a systematic evaluation based on ab initio calculations. *Energy Environ. Sci.* **2015**, *8*, 964–974.
- (6) Ponrouch, A.; Palacin, M. R. On the road toward calcium-based batteries. *Curr. Opin. Electrochem.* **2018**, *9*, 1–7.
- (7) Gummow, R. J.; Vamvounis, G.; Kannan, M. B.; He, Y. Calcium-Ion Batteries: Current State-of-the-Art and Future Perspectives. *Adv. Mater.* **2018**, *30*, No. 1801702.
- (8) Wang, D.; Gao, X.; Chen, Y.; Jin, L.; Kuss, C.; Bruce, P. G. Plating and stripping calcium in an organic electrolyte. *Nat. Mater.* **2018**, *17*, 16–20.
- (9) Ponrouch, A.; Frontera, C.; Barde, F.; Palacin, M. R. Towards a calcium-based rechargeable battery. *Nat. Mater.* **2016**, *15*, 169–72.
- (10) Li, Z.; Fuhr, O.; Fichtner, M.; Zhao-Karger, Z. Towards stable and efficient electrolytes for room-temperature rechargeable calcium batteries. *Energy Environ. Sci.* **2019**, *12*, 3496–3501.
- (11) Shyamsunder, A.; Blanc, L. E.; Assoud, A.; Nazar, L. F. Reversible Calcium Plating and Stripping at Room Temperature Using a Borate Salt. *ACS Energy Lett.* **2019**, *4*, 2271–2276.
- (12) Jie, Y.; Tan, Y.; Li, L.; Han, Y.; Xu, S.; Zhao, Z.; Cao, R.; Ren, X.; Huang, F.; Lei, Z.; Tao, G.; Zhang, G.; Jiao, S. Electrolyte Solvation Manipulation Enables Unprecedented Room-Temperature Calcium-Metal Batteries. *Angew. Chem., Int. Ed.* **2020**, *59*, 12689–12693.
- (13) Su, Z.; Ren, W.; Guo, H.; Peng, X.; Chen, X.; Zhao, C. Ultrahigh Areal Capacity Hydrogen-Ion Batteries with MoO<sub>3</sub> Loading Over 90 mg cm<sup>-2</sup>. *Adv. Funct. Mater.* **2020**, *30*, 2005477.
- (14) Wang, X.; Xie, Y.; Tang, K.; Wang, C.; Yan, C. Redox Chemistry of Molybdenum Trioxide for Ultrafast Hydrogen-Ion Storage. *Angew. Chem., Int. Ed.* **2018**, *57*, 11569–11573.
- (15) Tsumura, T.; Inagaki, M. Lithium insertion/extraction reaction on crystalline MoO<sub>3</sub>. *Solid State Ionics* **1997**, *104*, 183–189.
- (16) Hashem, A. M.; Askar, M. H.; Winter, M.; Albering, J. H.; Besenhard, J. O. Two-phase reaction mechanism during chemical lithium insertion into  $\alpha$ -MoO<sub>3</sub>. *Ionics* **2007**, *13*, 3–8.
- (17) Mai, L. Q.; Hu, B.; Chen, W.; Qi, Y. Y.; Lao, C. S.; Yang, R. S.; Dai, Y.; Wang, Z. L. Lithiated MoO<sub>3</sub> Nanobelts with Greatly Improved Performance for Lithium Batteries. *Adv. Mater.* **2007**, *19*, 3712–3716.
- (18) Hashem, A. M.; Groult, H.; Mauger, A.; Zaghbi, K.; Julien, C. M. Electrochemical properties of nanofibers  $\alpha$ -MoO<sub>3</sub> as cathode materials for Li batteries. *J. Power Sources* **2012**, *219*, 126–132.

(19) Zhou, L.; Yang, L.; Yuan, P.; Zou, J.; Wu, Y.; Yu, C. r-MoO<sub>3</sub> Nanobelts: A High Performance Cathode Material for Lithium Ion Batteries. *J. Phys. Chem. C* **2010**, *114*, 21868–21872.

(20) Gershinsky, G.; Yoo, H. D.; Gofer, Y.; Aurbach, D. Electrochemical and spectroscopic analysis of Mg<sup>2+</sup> intercalation into thin film electrodes of layered oxides: V<sub>2</sub>O<sub>5</sub> and MoO<sub>3</sub>. *Langmuir* **2013**, *29*, 10964–10972.

(21) Xiong, T.; Zhang, Y.; Wang, Y.; Lee, W. S. V.; Xue, J. Hexagonal MoO<sub>3</sub> as a zinc intercalation anode towards zinc metal-free zinc-ion batteries. *J. Mater. Chem. A* **2020**, *8*, 9006–9012.

(22) Liu, Y.; Wang, J.; Zeng, Y.; Liu, J.; Liu, X.; Lu, X. Interfacial Engineering Coupled Valence Tuning of MoO<sub>3</sub> Cathode for High-Capacity and High-Rate Fiber-Shaped Zinc-Ion Batteries. *Small* **2020**, *16*, No. 1907458.

(23) He, X.; Zhang, H.; Zhao, X.; Zhang, P.; Chen, M.; Zheng, Z.; Han, Z.; Zhu, T.; Tong, Y.; Lu, X. Stabilized Molybdenum Trioxide Nanowires as Novel Ultrahigh-Capacity Cathode for Rechargeable Zinc Ion Battery. *Adv. Sci.* **2019**, *6*, 1900151.

(24) Cabello, M.; Nacimiento, F.; Alcántara, R.; Lavela, P.; Pérez Vicente, C.; Tirado, J. L. Applicability of Molybdenite as an Electrode Material in Calcium Batteries: A Structural Study of Layer-type Ca<sub>x</sub>MoO<sub>3</sub>. *Chem. Mater.* **2018**, *30*, 5853–5861.

(25) Tojo, T.; Tawa, H.; Oshida, N.; Inada, R.; Sakurai, Y. Electrochemical characterization of a layered α-MoO<sub>3</sub> as a new cathode material for calcium ion batteries. *J. Electroanal. Chem.* **2018**, *825*, 51–56.

(26) Hannah, D. C.; Sai Gautam, G.; Canepa, P.; Ceder, G. On the Balance of Intercalation and Conversion Reactions in Battery Cathodes. *Adv. Energy Mater.* **2018**, *8*, 1800379.

(27) Blanc, L. E.; Sun, X.; Shyamsunder, A.; Duffort, V.; Nazar, L. F. Direct Nano-Synthesis Methods Notably Benefit Mg-Battery Cathode Performance. *Small Methods* **2020**, *4*, 2000029.

(28) Chen, W.; Zhan, X.; Luo, B.; Ou, Z.; Shih, P. C.; Yao, L.; Pidaparthi, S.; Patra, A.; An, H.; Braun, P. V.; Stephens, R. M.; Yang, H.; Zuo, J. M.; Chen, Q. Effects of Particle Size on Mg<sup>2+</sup> Ion Intercalation into λ-MnO<sub>2</sub> Cathode Materials. *Nano Lett.* **2019**, *19*, 4712–4720.

(29) Chae, M. S.; Kwak, H. H.; Hong, S.-T. Calcium Molybdenum Bronze as a Stable High-Capacity Cathode Material for Calcium-Ion Batteries. *ACS Appl. Energy Mater.* **2020**, *3*, 5107–5112.

(30) Kim, S.; Yin, L.; Lee, M. H.; Parajuli, P.; Blanc, L.; Fister, T. T.; Park, H.; Kwon, B. J.; Ingram, B. J.; Zapol, P.; Klie, R. F.; Kang, K.; Nazar, L. F.; Lapidus, S. H.; Vaughey, J. T. High-Voltage Phosphate Cathodes for Rechargeable Ca-Ion Batteries. *ACS Energy Lett.* **2020**, *5*, 3203–3211.

(31) Wustrow, A.; Hancock, J. C.; Incorvati, J. T.; Vaughey, J. T.; Poepfelmeier, K. R. Effect of Fluoride Doping on Lithium Diffusivity in Layered Molybdenum Oxide. *ACS Appl. Energy Mater.* **2019**, *2*, 2080–2086.

(32) Besenhard, J. O.; Heydecke, J.; Fritz, H. P. Characteristics of molybdenum oxide and chromium oxide cathodes in primary and secondary organic electrolyte lithium batteries. I. Morphology, structure and their changes during discharge and cycling. *Solid State Ionics* **1982**, *6*, 215–224.

(33) Gaillard, C.; Chevarier, N.; Den Auwer, C.; Millard-Pinard, N.; Delichere, P.; Sainsot, P. Study of mechanisms involved in thermal migration of molybdenum and rhenium in apatites. *J. Nucl. Mater.* **2001**, *299*, 43–52.

(34) Wen, B.; Chernova, N. A.; Zhang, R.; Wang, Q.; Omenya, F.; Fang, J.; Whittingham, M. S. Layered Molybdenum (Oxy)-Pyrophosphate as Cathode for Lithium-Ion Batteries. *Chem. Mater.* **2013**, *25*, 3513–3521.

(35) Bak, S.-M.; Qiao, R.; Yang, W.; Lee, S.; Yu, X.; Anasori, B.; Lee, H.; Gogotsi, Y.; Yang, X.-Q. Na-Ion Intercalation and Charge Storage Mechanism in 2D Vanadium Carbide. *Adv. Energy Mater.* **2017**, *7*, 1700959.

(36) Kang, J.-H.; Paek, S.-M.; Choy, J.-H. In Situ X-ray Absorption Spectroscopic Study for α-MoO<sub>3</sub> Electrode upon Discharge/Charge

Reaction in Lithium Secondary Batteries. *Bull. Korean Chem. Soc.* **2010**, *31*, 3675–3678.

(37) Sowrey, F. E.; Skipper, L. J.; Pickup, D. M.; Drake, K. O.; Lin, Z.; Smith, M. E.; Newport, R. J. Systematic empirical analysis of calcium–oxygen coordination environment by calcium K-edge XANES. *Phys. Chem. Chem. Phys.* **2004**, *6*, 188–192.

(38) Rodriguez, J. A.; Wang, X. Q.; Hanson, J. C.; Liu, G.; Iglesias-Juez, A.; Fernandez-Garcia, M. The behavior of mixed-metal oxides: Structural and electronic properties of Ce<sub>1-x</sub>Ca<sub>x</sub>O<sub>2</sub> and Ce<sub>1-x</sub>Ca<sub>x</sub>O<sub>2-x</sub>. *J. Chem. Phys.* **2003**, *119*, 5659–5669.

## Recommended by ACS

### Efficacy of Stabilizing Calcium Battery Electrolytes through Salt-Directed Coordination Change

Nathan T. Hahn, Kevin R. Zavadil, *et al.*

JUNE 14, 2022  
THE JOURNAL OF PHYSICAL CHEMISTRY C

READ 

### Spectroscopic Insights into the Electrochemical Mechanism of Rechargeable Calcium/Sulfur Batteries

Antonio Scafuri, Lorenzo Stievano, *et al.*

SEPTEMBER 16, 2020  
CHEMISTRY OF MATERIALS

READ 

### Reversible Calcium-Ion Insertion in NASICON-Type NaV<sub>2</sub>(PO<sub>4</sub>)<sub>3</sub>

Boosik Jeon, Seung-Tae Hong, *et al.*

SEPTEMBER 23, 2020  
CHEMISTRY OF MATERIALS

READ 

### Development of the Ca/FeS<sub>2</sub> Chemistry for Thermal Batteries

Stewart A. M. Dickson, John T. S. Irvine, *et al.*

SEPTEMBER 09, 2021  
CHEMISTRY OF MATERIALS

READ 

Get More Suggestions >